An Examination of the Effect of Trailing Edge Flaps on Swashplateless Rotor Performance

Jaye Falls
falls@usna.edu
Asst. Research Professor
Dept. of Ocean Eng.
U.S. Naval Academy

Anubhav Datta
datta@merlin.arc.nasa.gov
Rotorcraft Dynamicist
ELORET Corp.
NASA Ames Research Center

Inderjit Chopra
chopra@umd.edu
Alfred Gessow Professor and Director
Alfred Gessow Rotorcraft Center
University of Maryland

ABSTRACT

This paper evaluates the effect of trailing edge flaps on swashplateless rotor performance in hover and in forward flight. The baseline rotor to which the performance predictions are compared is the UH-60A. The swashplateless variant maintains similar hub and blade properties with a reduced torsional frequency and the addition of an integrated trailing edge flap on each blade. The comprehensive analysis includes the inertial and aerodynamic contributions of the trailing edge flaps. In hover, thrust sweeps of the swashplateless rotor show that high index angle increases the figure of merit compared to the baseline rotor for a small range of thrust. In forward flight, two different wake vorticity patterns, the first a single blade tip vortex and the second a tip vortex plus trailed vortices at the span-wise edges of the flap, are used to demonstrate the sensitivity of the performance prediction to the wake. Using full vehicle trim and the second of the two wake patterns, the swashplateless rotor power prediction is 1% lower than the baseline at low speed, $\mu = 0.16$, and increases to 11% higher than the baseline at $\mu = 0.30$. Reducing the equivalent flat plate area of the swashplateless rotor by 20% to simulate the removal of the swashplate leads to a decrease of 5% in the power prediction across the range of forward flight speed, compared to the baseline.

INTRODUCTION

A comprehensive analysis is developed to analyze the effect of integrated trailing edge flaps (TEFs) on swashplateless rotor performance in hover and in forward flight. A previously designed swashplateless variant of a UH-60A rotor [1, 2] is examined and compared to wind tunnel and flight test data for the UH-60A rotor baseline, with an emphasis on main rotor power and rotor lift-to-drag ratio.

The trailing edge flaps that are the subject of this investigation are integrated into the blade profile, producing lift and moment for blade pitch control with a minimum of profile drag compared to external servo-flaps. However, integrated flaps have limited authority to control blade pitch because the limited length available for moment arm constrains the pitch moment produced by the flap deflections. It is therefore necessary to establish the impact on rotor torque of the large flap deflections required to trim a swashplateless rotor. The feasibility of integrated trailing edge flaps for primary control depends in part on the torque required to trim the rotor, which should be close to or below that required for conventional swashplate control in hover and in forward flight.

Previous investigations of the effect that trailing edge flaps have on performance have been in the context of vibration control. Experimental studies by Noonan [3] on the HIMARCS (High Maneuverability and Agility Rotor and Control System) rotor showed performance improvements could be achieved with slats or flaps. Most recent investigations have been numerical. Studying the HIMARCS rotor, Gagliardi [4] found that combinations of steady flap deflections and low twist rotor blades can improve conventional rotor performance in hover and in forward flight. Numerical investigations of active/passive optimization by Glaz and Friedmann [5] and Liu *et al.* [6] examined simultaneous vibration control and performance improvement with trailing edge flaps. Yeo compared seven active controls in their effect on rotor performance: IBC, trailing edge flap, active twist, oscillatory jet, Gurney flap, leading edge droop, leading edge slat [7]. These controls are commonly used for vibration or noise control, but in that work only performance impact was studied.

In the present work, trailing edge flaps are used for primary control of a swashplateless rotor. The focus of the investigation is the effect of those flaps on swashplateless rotor performance in comparison to a baseline, conventional rotor.

APPROACH

First, a baseline model was developed and validated for the UH-60A rotor. This rotor was chosen as an example of a current production rotor with extensive test data available for validation of analytical predictions. A swashplateless variant of the model was created while maintaining similar blade properties. A comprehensive analysis was developed which includes trailing edge flap inertia and aerodynamics. In previous work [8], a design was produced for the swashplateless rotor which could be trimmed in hover and across the range of forward flight speed with moderate flap angles and hinge moments. These operating conditions are necessary to minimize the actuator power required to drive the flaps. The resulting trailing edge flap was 0.15c in size, and spanned 0.40 of the blade radius. The center of the flap was placed at 0.75R. The aerodynamic balance that was found to be advantageous for the reduction of trailing flap hinge moment is omitted to facilitate the generation of aerodynamic properties for the flapped airfoil.

The trailing edge flaps used to control the rotor alter

the 2D airfoil lift, drag and moment properties on the blade sections where the flap is located. Therefore, aerodynamic properties were generated for a flapped version of the SC1094R8 airfoil using a computational fluid dynamics (CFD) analysis. The flap deflections also are assumed to alter the rotor wake. Accordingly, two different vorticity patterns were used for the free wake model. The first pattern represents the far wake as rolled up into a single vortex trailed from the blade tip, and is identical to that used for the baseline rotor. The flaps are not considered in the either the near or far wake calculations. The second pattern includes the effect of the trailing edge flaps in both the near and far wake, and adds two additional trailers to the blade wake, produced at the inboard and outboard edges of the deflected flap.

Next, the baseline and swashplateless rotors were compared in various flight conditions. In hover, torque and figure of merit were calculated for a range of thrust, and the effect of blade index angle on the performance of the swashplateless rotor was assessed. In forward flight, the torque required for the swashplateless rotor was predicted using both wake patterns, and compared to the baseline rotor. The differences in the power predictions produced by these two patterns were studied by examining the blade angle of attack in some detail.

Finally, using the second wake pattern, the effect on swashplateless rotor performance of increasing thrust or decreasing parasitic drag were studied across the range of forward flight speed.

ANALYSIS METHODOLOGY

Rotor Model

In order to implement swashplateless control, the baseline rotor is modified to remove the pitch link and replaced it with a soft torsion spring. The rotor and blade properties are the same as the UH-60A helicopter, except that the first torsion frequency is now reduced from 4.38/rev (baseline) to 1.92/rev (swashplateless). The rotor is modeled in the University of Maryland Advanced Rotorcraft Code (UMARC) with a single main rotor and a tail rotor. Each of the four articulated blades has coincident flap and lag hinges at 4.66% span, and a 26.83 ft radius with an aerodynamic root cutout of 20%. The nominal chord of the blades is 1.73 ft. The rotor speed is 258 RPM. The blades are discretized into 20 finite elements with flap, lag, torsion and axial degrees of freedom. Fig. 1a shows the discretization of the blade. The tip sweep in the outer 6.9% of the blade span (reaching a maximum of 20 at 94.5% span) is modeled as structural (center of gravity) and aerodynamic (aerodynamic center) offsets from a straight, undeformed elastic axis. The baseline aerodynamic, trim and structural models have been validated against flight test data [9, 10]. The second order nonlinear beam formulation, based on Refs. [11] and [12], is modified to integrate the structural, inertial and aerodynamic contributions of the trailing edge flap. The flap is modeled as an additional single degree of freedom, but for the trim problem, the control flap motions are prescribed. Although the flap can be defined across multiple elements with varying properties, the motion is described by a single deflection. The baseline unsteady aerodynamic formulation for the trailing edge flap is based on thin airfoil theory [13], and includes an arbitrary hinge axis for the flap, with gaps assumed sealed. For the baseline rotor, inflow is calculated using a refined Bagai-Leishman pseudo-implicit free wake model with a single vortex at the tip of the rotor blade.

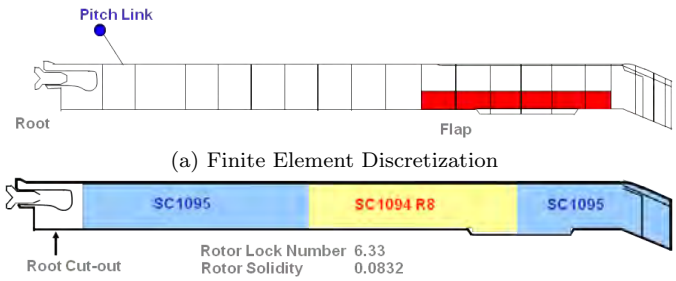

(a) Finite Element Discretization

(b) Airfoil Distribution

Figure 1: Rotor Blade Planform, Showing Finite Elements, Airfoils, and Trailing Edge Flap Location

Drag of Trailing Edge Flaps

Published aerodynamic data for airfoils with trailing edge flaps is limited, especially drag data. For flapped airfoils, there is insufficient published data to construct a full C81 aerodynamics table. Within the comprehensive analysis, airfoil tables for the SC1095 and SC1094R8 sections are used to calculate the performance baseline. CFD analysis is used to provide aerodynamic data for the SC1094R8 with a 0.15c flap; the CFD predictions for zero flap deflection will be compared to test data for validation of the baseline airfoil.

The SC1095R8 airfoil is examined using a two dimensional Navier-Stokes CFD code (TURNS) to produce aerodynamic properties over a range of angles of attack, Mach number, and flap deflection. The CFD computations are performed using the overset structured mesh solver OVERTURNS [14]. This code solves the compressible RANS equations using a diagonal form of the implicit approximate factorization method developed by Pulliam and Chaussee [15]. The Spalart-Allmaras [16] turbulence model is employed for the RANS closure. The code was validated against test data and other CFD analyses [17] for the SC1095 airfoil. The trailing edge flap is hinged at the leading edge, and is modeled with no gap. The flap chord length is 0.15c. The baseline airfoil is the SC1094R8 with zero flap deflection.

The lift, drag and pitch moment coefficients for the baseline prediction are compared to test data at Mach number of 0.3 (See Fig. 2). At positive angles of attack, the CFD prediction of drag matches the test data within 5%, except for the region from 12° to 16°. For the negative angles of attack, accuracy is within 5% from 0° to -4°. Beyond -4°, the slope of the prediction follows the test data closely, but the magnitude differs significantly. The CFD prediction of lift matches test data within 5%, for angles of attack between -10° and 14°. For positive angles of attack, the trend of the prediction follows the data closely. On the negative side, the prediction diverges from test data at -10°. The pitch moment prediction follows the trends of the test data closely within the angle of attack bounds

defined for lift.

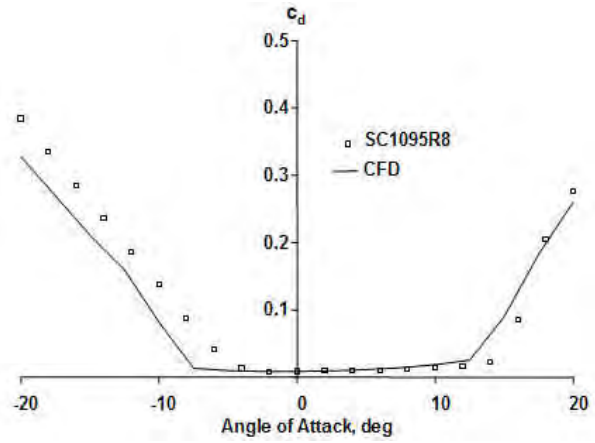

(a) Drag Coefficient

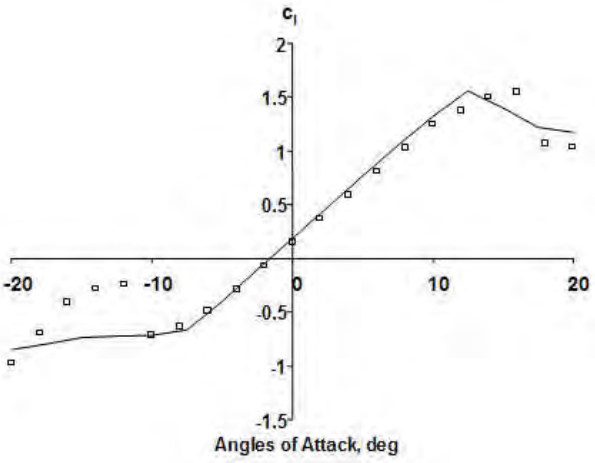

(b) Lift Coefficient

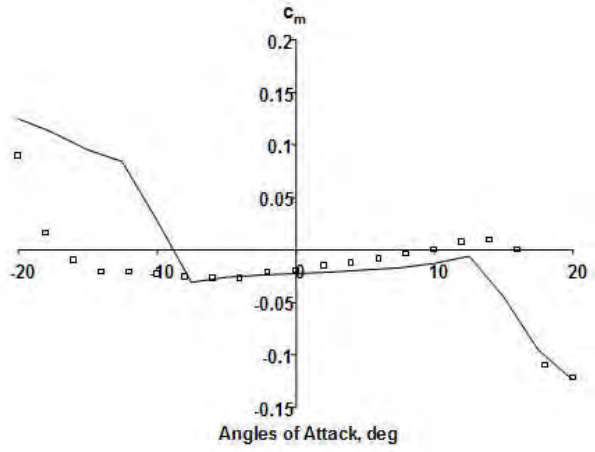

(c) Pitch Moment Coefficient

Figure 2: Comparison of CFD Predicted and Measured Baseline SC1094R8 Airfoil Properties at M = 0.3, No Flap.

The drag prediction for the flapped airfoil follows the trends established in wind tunnel tests of the HH-06 [18]: at positive angles of attack, a negative (upward) TEF deflection reduces the airfoil drag, while positive (downward) TEF deflection increases the drag. The reverse occurs for negative angles of attack. Figure 3 shows the drag predictions for TEF deflections of ±10° on the SC1094R8. Using the aerodynamic properties thus generated, lookup tables were constructed for a full range of angle of attack, for Mach number between 0.3 and 0.8, and for flap deflections from −15° to +15°.

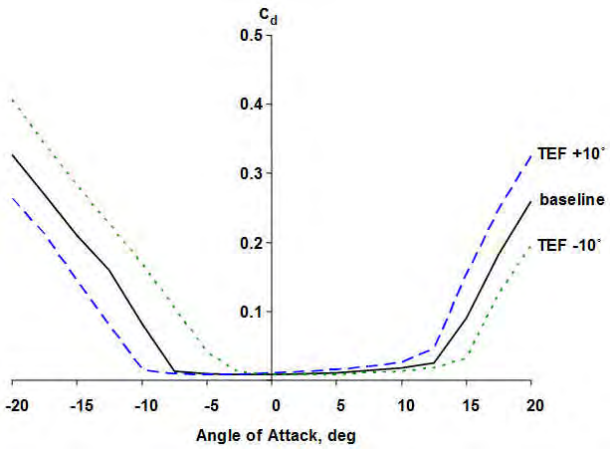

Figure 3: CFD Drag Prediction for ±10° TEF Deflection for Flapped SC1094R8, $c_f = 0.15c$, No Overhang, M = 0.3

Inflow and Wake Model

A refined wake roll-up is proposed which includes the trailing edge flap in the near and far wake calculations by assuming small interruptions to the flow at the inboard and outboard bounds of the flap. The baseline wake model uses a fully rolled-up free tip vortex, developed by Bagai and Leishman [19]. An iterative procedure is used to calculate bound circulation strengths for the near and far wake. The near wake model is based on the Weissinger-L lifting line theory. Initially, sectional angles of attack along the blade are calculated using blade deformations and uniform inflow, and are used to extract lift coefficients from the 2D airfoil tables. The first estimate of the bound circulation strengths is derived from the lift using the Kutta-Joukowski theorem. The far wake is based on the bound circulation strengths, and produces a non-uniform inflow distribution which is used to re-calculate the sectional angles of attack. The new angles of attack enter the near wake model and result in revised bound circulation strengths for the far wake. A converged wake solution results in bound circulation strengths that are consistent for the airfoil tables, the near wake and the far wake. The strength across each element is assumed constant. The shed vortex at the blade tip is assigned a circulation strength corresponding to the maximum bound circulation outboard of 0.5R on the blade. This is based on the assumption that all of the circulation outboard of that point rolls up into the tip vortex. The refined wake roll-up assumes that in addition to the tip vortex, vortices are trailed at the radial bounds of the flap. With the periodic oscillation of the flap, gaps appear at the inboard and outboard flap edges. It is suggested that these gaps cause interruptions in the flow that can produce small trailers at the flap bounds. The strength of each flap trailer is calculated as the difference between the strengths of the elements neighboring the gap. The circulation strength of the tip vortex is the peak circulation outboard of 0.5R, less the contribution of the two flap trailers. Fig. 4b shows a schematic of the new wake model.

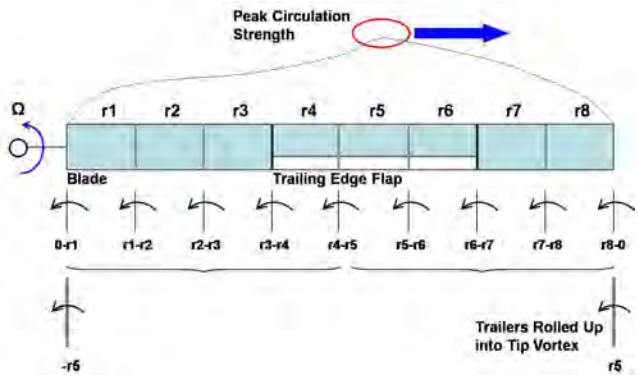

(a) Tip Vortex Model

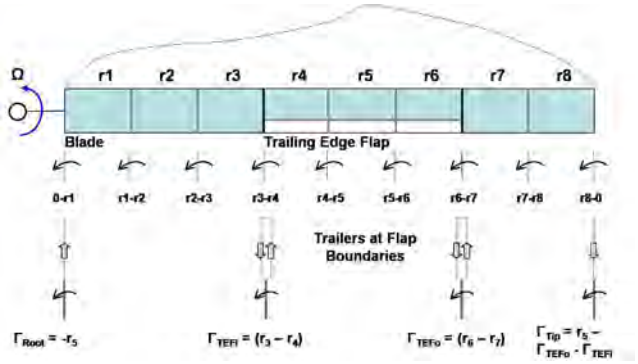

(b) TEF Trailers Model

Figure 4: Schematics of Trailed Wake Patterns for Swashplateless Rotor Model

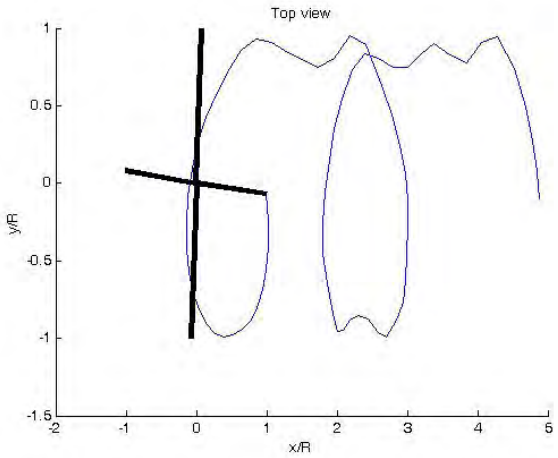

(a) Single Tip Vortex

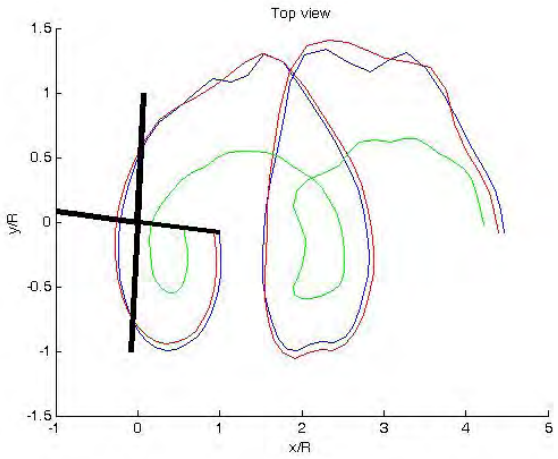

(b) TEF Trailers

Figure 5: Effect of Wake Pattern on Swashplateless Predicted Power in Forward Flight, $C_W/\sigma = 0.0783$, $\mu = 0.27$

The two wake roll-up patterns can be seen in Fig. 5. Figure 5a shows the tip vortex trailed from one blade of the swashplateless rotor through two turns. The TEF trailers added to the wake are shown in Fig. 5b.

RESULTS IN HOVER

The baseline and swashplateless rotors are trimmed to zero hub moments and a target thrust level, C_T/σ. The shaft angles for both the baseline and swashplateless rotor are set to zero, with the tail rotor collective at 6°. The control pitch angles are replaced with control flap angles for the swashplateless rotor. The configuration used in this investigation is a TEF with chord of 0.15c and 0.40R span, with the midpoint located at the 75% radial station. The flap hinge is located at its leading edge, so that it has no aerodynamic overhang.

The hover analysis is conducted with uniform inflow, using lookup tables for both the main blade and the trailing edge flap aerodynamics. The primary focus of the hover analysis is determining the effect of index angle on the predicted power. The baseline power and Figure of Merit (FM) for the UH-60A were shown in Figures 6 and 7. The range of index angle for the swashplateless rotor was varied from 5° to 19° and the thrust sweep, C_T/σ, was from 0.01 to 0.09. For each index angle, the swashplateless rotor was examined at increasing values of thrust, until blade deflection diverged and trim solutions were no longer found. The maximum thrust level achieved at each index angle decreases as the index angle decreases.

For all results in this investigation, the index angle of the swashplateless rotor is not a degree of freedom, but is a prescribed value held constant for a range of thrust (in hover) or speed (in forward flight). Since the index angle is held constant for all of the results presented in this investigation, an angle was selected to minimize the required control angles and hinge moments at the most demanding flight condition: high speed, with the weight condition corresponding to $C_W/\sigma = 0.0783$. Ideally, the index angle would decrease with thrust as the pitch collective does for the conventional rotor.

Figure 8 shows that the required power decreases as the index angle increases from 5° to 15°. From $C_T/\sigma = 0.01$ to 0.05, the power predictions for the baseline and swashplateless rotors are very similar, for all index angles. As the thrust increases above 0.05, differences can be seen. For 5° index, the predicted power increases rapidly from $C_T/\sigma = 0.05$ to 0.07, reaching a maximum at $C_T/\sigma = 0.07$. Above that level of thrust, a trim solution could not be found. At 10° index, the rapid increase in predicted power previously seen for the lower index angle does not occur until the thrust reaches 0.07. At 15° index angle, the power prediction is slightly lower than the baseline rotor for $C_T/\sigma = 0.05$ to 0.08. Finally, the highest index angle analyzed is 20°, where the power prediction dips below the conventional rotor from $C_T/\sigma = 0.05$ to 0.10. As the thrust continues to increase, the power for 20° index be-

gins to cross the baseline prediction, following a trend similar to that shown by the lower index angles. The curve is not fully expressed, however, as blade deflections diverged for this configuration above $C_T/\sigma = 0.10$.

Figure of merit (FM) offers another perspective on the trends of predicted power in Figure 9. The curve for 5° index follows the baseline prediction until $C_T/\sigma = 0.05$. Above that level of thrust, the FM decreases abruptly. At higher index angles, the FM of the swashplateless rotor exceeds that of the baseline, and the peak value of FM and the thrust at which it occurs increase with increasing index angle. For the 20° index, the most improvement in FM occurs at $C_T/\sigma = 0.08$, where the swashplateless rotor shows a 14% increase in efficiency. The blade angle of attack at 0.75R increases as the index angle decreases in Figure 10. As the thrust increases, the angle of attack increases more rapidly for the swashplateless rotor than for the conventional. The flap deflections corresponding to these predictions are shown in Figure 11. It can be seen that for every index angle, at all thrust levels above $C_T/\sigma = 0.03$, the flap angle needed to trim is negative (upward), and becomes more negative nearly linearly as the thrust increases. This flap deflection produces negative lift which is counteracted by the increased blade angle of attack.

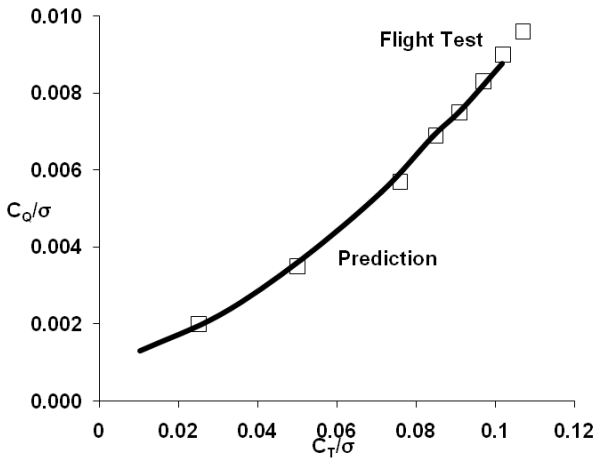

Figure 6: Predicted and Measured Power for UH-60A in Hover, Uniform Inflow

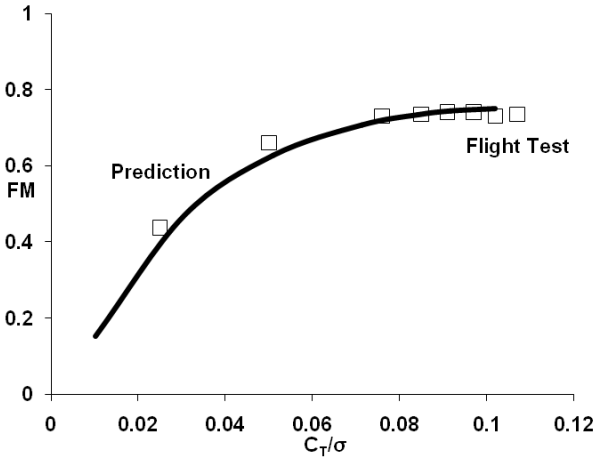

Figure 7: Predicted and Measured Figure of Merit for UH-60A in Hover, Uniform Inflow

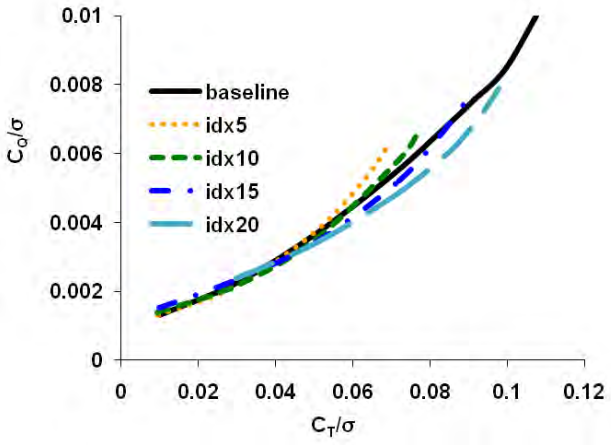

Figure 8: Effect of Index Angle (idx) on Predicted Power, in Hover

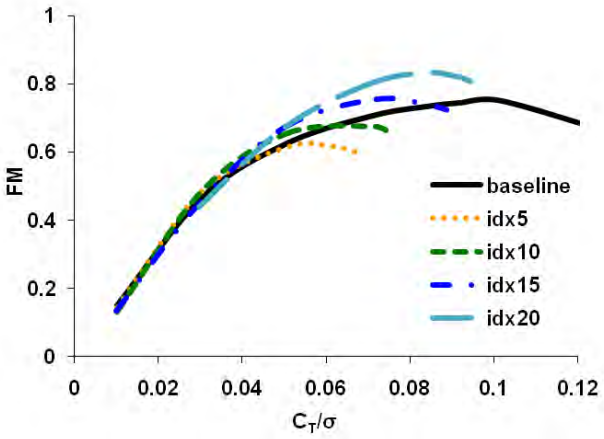

Figure 9: Effect of Index Angle on Figure of Merit

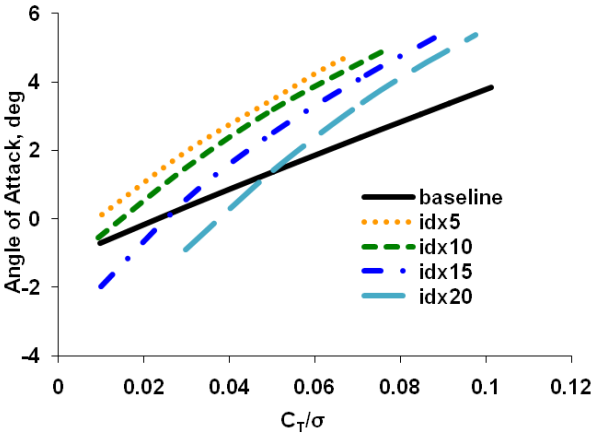

Figure 10: Effect of Index Angle on Blade Angle of Attack at 75%R, in Hover

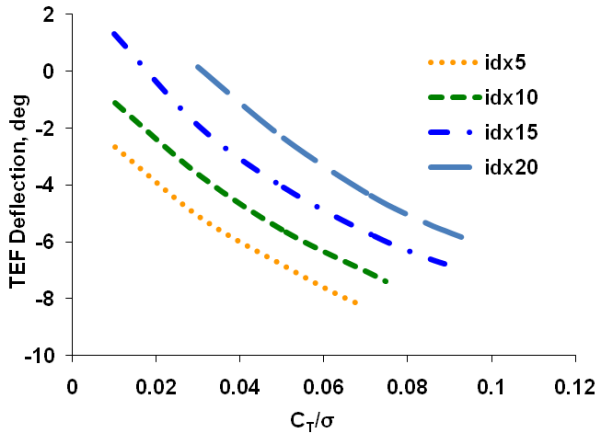

Figure 11: Effect of Index Angle on Required TEF Deflection, in Hover

RESULTS IN FORWARD FLIGHT

The forward flight analysis includes equivalent flat plate area as an estimate of the parasitic drag of the fuselage; in combination with the airfoil aerodynamics, this results in a required thrust for a given C_W/σ and flight speed. For each speed examined in this investigation, the swashplateless and baseline rotors are trimmed to matching thrust levels. By keeping the flat plate area the same for the baseline and swashplateless helicopter models, a disadvantage is conferred upon the swashplateless model, when in reality the absence of the swashplate would reduce the parasitic drag. An attempt has not been made to estimate the parasitic drag of the swashplate for this investigation.

Effect of Wake Model

In this section, the effect of the wake model on the prediction of conventional and swashplateless rotor power is studied by examining both the values and trends of the power. First, the power predictions for the baseline rotor are validated against flight test data.

The power and longitudinal shaft predictions for the baseline rotor are produced with the single tip vortex free wake model and a six degree of freedom vehicle trim. These predictions compare well to flight test data obtained from the NASA/Army UH-60A Airloads Program (stored in the NASA Ames Research Center database). The baseline is established for a nominal vehicle weight coefficient, C_W/σ, of 0.0783, which corresponds to a vehicle gross weight of 16500 lbs. The predicted shaft angles shown in Fig. 12 compare well to flight test data at speeds above $\mu = 0.32$. Below that speed, the predicted angles follow the trend of the test data. The prediction of required power, C_Q/σ is compared to flight test data across a range of flight speeds in Fig. 13. The predicted results are accurate to within 2% of measured data. Removing the free wake from the model, and using uniform inflow only causes the power prediction to shift downward; however, the predictions with uniform inflow follow the trend of the test data for a conventional rotor, an indication that comparisons of predictions made with uniform inflow may yield correct trends for the swashplateless rotor too.

All forward flight cases for the swashplateless rotor and the conventional rotor with uniform inflow use a moment trim targeted to zero hub moments. The shaft angles are prescribed to match those of the baseline rotor at the same speed. The index angle of the swashplateless rotor is set to 15°. The aerodynamic lookup tables for the trailing edge flaps contain properties for flap deflections of 0°, ±10° and ±15°, generated by the CFD analysis described previously. The lookup is based on linearly interpolated values of Mach number, angle of attack, and TEF deflection. Extrapolation up to 4° beyond the available TEF data is used in the prediction. The interpolation and extrapolation relies upon the assumption that the values of c_l, c_d, c_m, and c_h are close to linear between the existing data points. This appears to be an acceptable assumption for Mach number and angle of attack where many data points spanning a broad range are available; it may not be appropriate for the trailing edge flap at large flap deflections, where some effects of flow separation might be expected, but not captured. Solutions are found using both uniform inflow and the free wake. The free wake model has one vortex shed at the tip of the blade, with peak circulation strength at each azimuth angle.

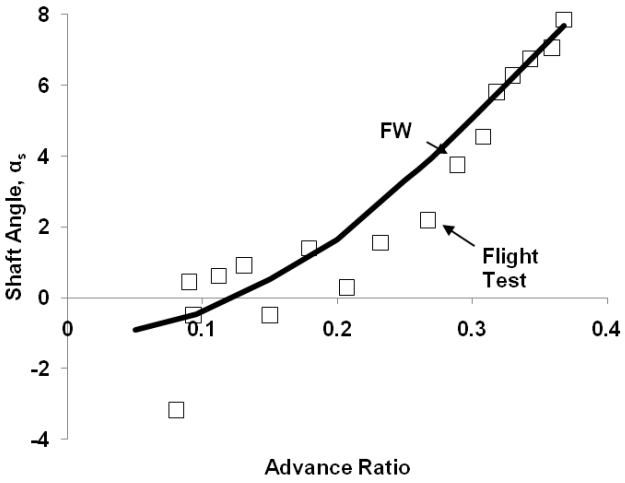

Figure 12: Predicted and Measured Shaft Angles for UH-60A in Forward Flight, $C_W/\sigma = 0.0783$ (FW: free wake)

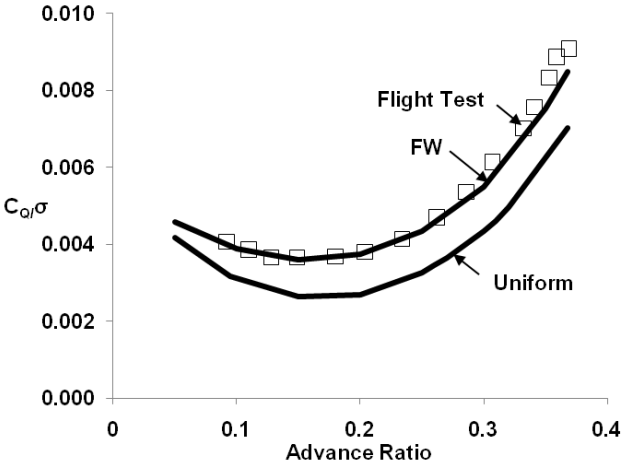

Figure 13: Predicted and Measured Power for UH-60A in Forward Flight, $C_W/\sigma = 0.0783$ (FW: free wake, Uniform: uniform inflow)

Using uniform inflow, the predicted power for the swash-

plateless rotor with 15° index follows the baseline prediction from $\mu = 0.11$ to $\mu = 0.25$ (see Figure 14). As the advance ratio increases beyond 0.25, the swashplateless power prediction begins to diverge from the baseline, increasing rapidly until $\mu = 0.30$, where the swashplateless power is 33% higher than the baseline rotor. Beyond that speed, the trim solution diverges for the swashplateless rotor.

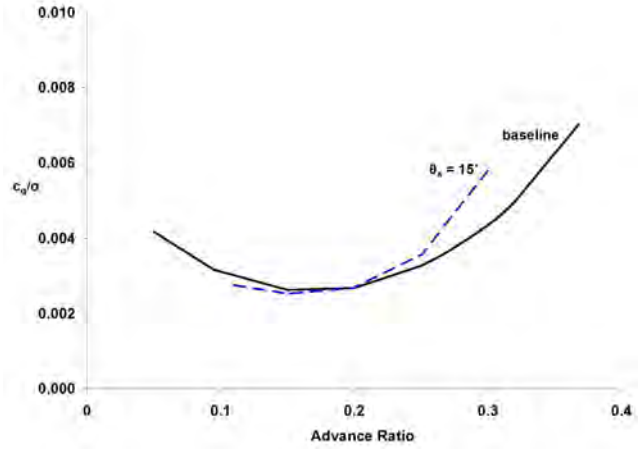

Figure 14: Predicted Power in Forward Flight, $C_W/\sigma = 0.0783$, Uniform Inflow

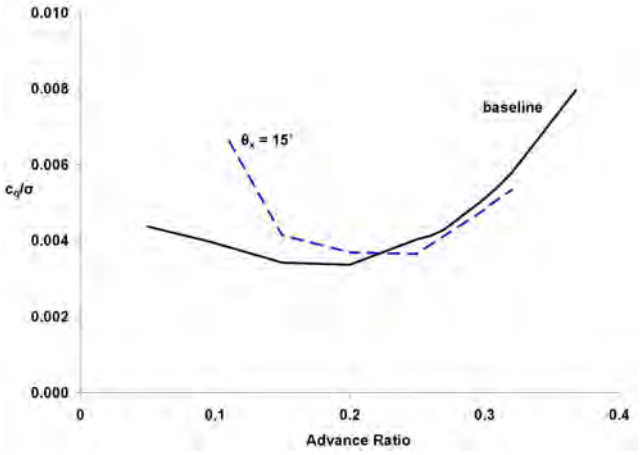

Figure 15: Predicted Power in Forward Flight, $C_W/\sigma = 0.0783$, Free Wake

A similar divergence phenomenon is observed when the analysis incorporates the free wake, but at low speed instead of high. Figure 15 shows the swashplateless power prediction following the baseline within the range $\mu = 0.2$ to $\mu = 0.30$. The swashplateless power diverges from the baseline prediction at low speed ($\mu = 0.15$), where the 15° index angle requires 21% more in power. The prediction continues to increase as the flight speed decreases; blade divergence occurred between $\mu = 0.11$ and hover. Above $\mu = 0.30$, blade deflection diverges again. The mean flap control angles corresponding to the predicted power are shown in Fig. 16. The flap deflections required for trim are negative for the range of flight speed. The swashplateless power predictions are very sensitive to the inflow model; omitting the free wake changes the required flap deflection for trim by up to 100%. For example, at low speed, $\mu = 0.11$, the flap deflection required for trim is -4°

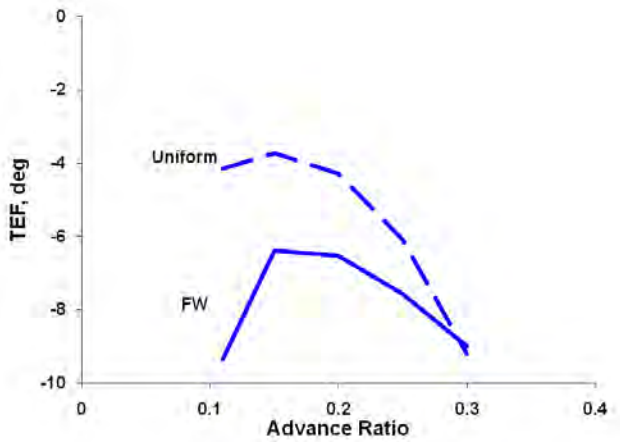

Figure 16: Mean Flap Control Angles in Forward Flight, $C_W/\sigma = 0.0783$, Uniform and Free Wake Inflow

for uniform inflow, and -8.5° for free wake. Looking in the middle of the range, at $\mu = 0.25$, the TEF deflection is -6° for uniform inflow, and -7.5° for free wake. From this it can be concluded that neglecting the free wake in analysis underestimates the power and required flap deflection for a given thrust, in steady level flight.

The results discussed in the preceding sections use the baseline wake model without any modification for the trailing edge flap. This means that the sectional angles of attack do not include the effect of the flap, and the near and far wake are calculated as they would be for an unflapped blade. A revision to the wake model is proposed which includes the trailing edge flap in the near and far wake calculations by assuming small interruptions to the flow at the inboard and outboard bounds of the flap. The trim solution for the swashplateless rotor is a three degree of freedom solution, with targeted thrust and zero hub moments; the longitudinal and lateral shaft angles, plus the tail rotor collective, match those of the conventional rotor at each advance ratio. The trim solution for the conventional rotor is full vehicle trim with six degrees of freedom. The power predicted with the TEF trailer wake model follows the trend of the baseline rotor power prediction for the range of advance ratio from $\mu = 0.11$ to $\mu = 0.30$, as shown in Fig.17. In Figure 17a, at low speed transition ($\mu = 0.11$), the predicted power for the swashplateless rotor has decreased to 15% below the baseline rotor, using the refined wake model. As the advance ratio increases to $\mu = 0.25$, the swashplateless prediction approaches the baseline power. From $\mu = 0.25$ to $\mu = 0.30$, the swashplateless power prediction increases to 10% above the baseline rotor. This represents a large change from the swashplateless power predicted by the tip vortex model, particularly in the low speed range from $\mu = 0.25$ to $\mu = 0.11$. The trends of the power predictions from the two wake models are divergent at this speed. The tip vortex model is above the baseline at $\mu = 0.15$, and increases sharply to $\mu = 0.11$. In contrast, the TEF trailer model predicts power below the baseline at $\mu = 0.15$, and follows the trend of the baseline power prediction to $\mu = 0.11$. Figure 17b compares the swashplateless power predictions from the refined free wake model to uniform inflow and the baseline rotor. For both inflow models, the swashplateless power prediction follows the trend of the baseline rotor;

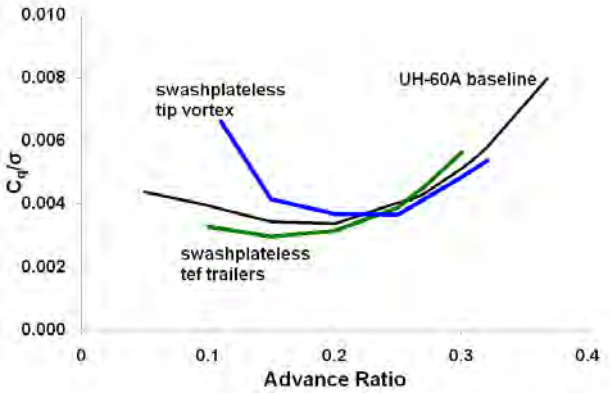

(a) TEF Trailers Compared to Tip Vortex Model

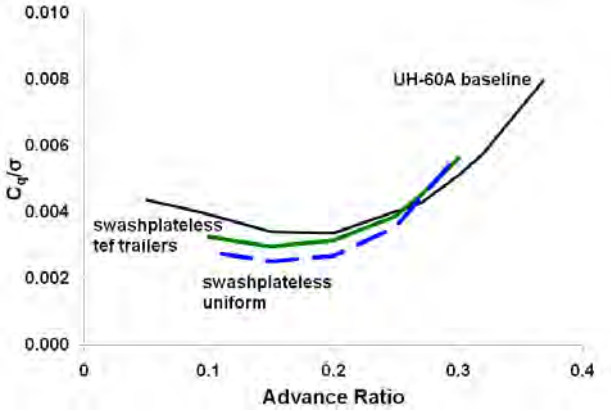

(b) TEF Trailers Compared to Uniform Inflow

Figure 17: Effect of Free Wake Model on Predicted Power in Forward Flight, $C_W/\sigma = 0.0783$

however, the refined free wake model predicts higher rotor power from $\mu = 0.10$ to 0.25.

Detailed Study of Blade Angle of Attack

To understand the power predictions produced by the different wake voticity patterns, the details of angle of attack are shown for azimuth and Mach number at low speed (μ = 0.11), where the swashplateless predictions from the tip vortex and TEF trailer models diverge.

At low speed, $\mu = 0.11$, strong vortex interaction takes place and the free wake is necessary for correct prediction of the angle of attack. The shaft angle at this speed is nearly vertical at -0.20°. Figure 18 shows the two free wake predictions for the swashplateless rotor and compares them to the baseline rotor. The power prediction from the tip vortex free wake model is affected by a 5° increase in angle of attack seen by the swashplateless rotor compared to the baseline at 0.75R. The TEF trailer free wake model predicts no increase in maximum angle of attack at this station and a small decrease in the power prediction. Figure 19 shows the angle of attack vs. Mach number envelope for both wake models for the swashplateless rotor. The original wake model resulted in a trim solution where the angles of attack on the retreating side of the disk were near the stall boundary of the airfoil. The TEF trailer model prediction has reduced the angles of attack for the swashplateless rotor so that they remain within the static stall boundary at this section.

In Figure 20 the lift-drag envelope for the TEF trailer

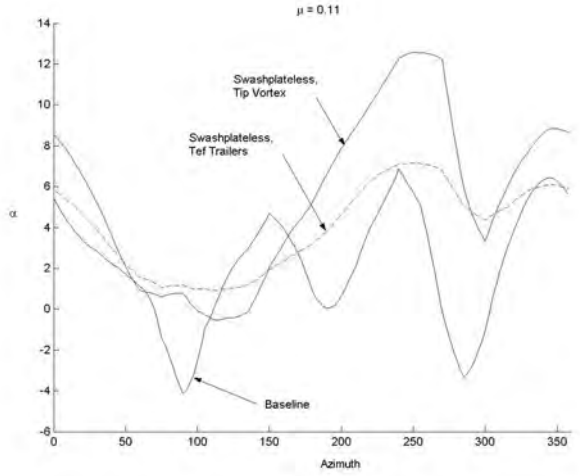

Figure 18: Angle of Attack vs. Azimuth, Baseline and Swashplateless Rotors, Tip Vortex and TEF Trailer Wake Models, for $\mu = 0.11$ at 0.75R

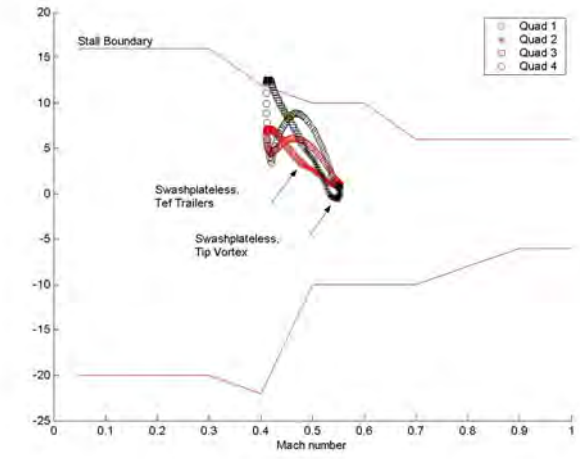

Figure 19: Angle of Attack vs Mach Number, Swashplateless Rotor, TEF Trailer Wake Model, for $\mu = 0.11$ at 0.75R

wake model is smooth and compact, reflecting the small range of angles of attack predicted for this section. The lift-drag envelope predicted by the tip vortex wake model has a maximum drag coefficient that is 5 times larger than the revised wake model, which contributes to the much larger power prediction. Although the trend of the TEF deflections are similar for both wake models, seen in Figure 21, the range of motion varies greatly. The tip vortex free wake results in more than 20° of TEF deflection, while the range of TEF deflection for the revised wake model is reduced to 7°. The very large negative trailing edge flap deflection predicted by the tip vortex model causes a lift decrement. For the swashplateless rotor to trim at the same thrust level as the baseline, there is a compensating large increase in blade angle of attack. As a result, the rotor performance is degraded. The reduction of TEF deflection that accompanies the TEF trailer wake model eliminates the increase in the blade angle of attack, and thus the performance prediction improves.

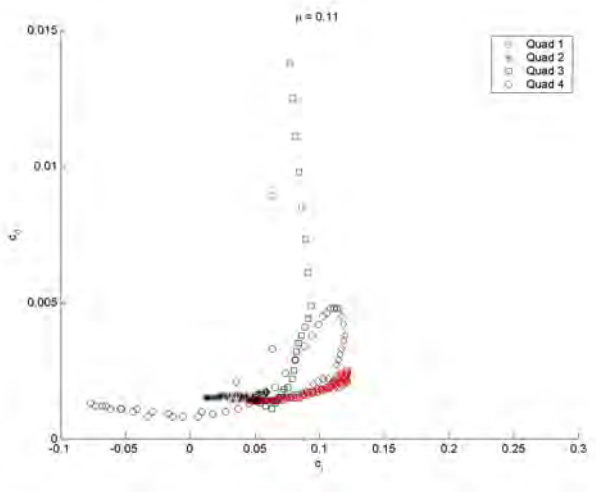

Figure 20: Lift and Drag Envelope, Swashplateless Rotor, TEF Trailer Wake Model, for $\mu = 0.11$ at 0.75R

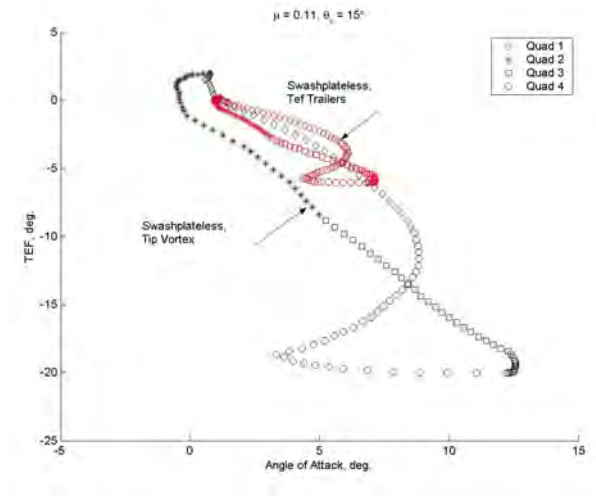

Figure 21: TEF vs. Angle of Attack, Swashplateless Rotor, Tip Vortex and TEF Trailer Wake Models, for $\mu = 0.11$ at 0.75R

Effect of Thrust on Swashplateless Rotor

Having refined the wake model to reflect the probable physics of the flapped blade, the performance predictions in forward flight are re-evaluated using full vehicle (6 dof) trim. For the swashplateless rotor, the six trim variables are: the flap collective (mean deflection), the two flap cyclics, the shaft lateral and longitudinal positions, and the tail rotor collective. The swashplateless rotor is compared to the baseline in Fig. 22a, across the range of forward flight speeds. The swashplateless power follows the baseline prediction from $\mu = 0.16$ to $\mu = 0.30$ more closely than the results obtained using the 3dof trim. Compared to the baseline, there is a moderate increase in the swashplateless power prediction from $\mu = 0.25$ to $\mu = 0.30$, so that at $\mu = 0.30$, the predicted swashplateless power is 11% higher than the baseline. At low speed, the swashplateless power is reduced 1% from the baseline prediction at $\mu = 0.16$. The predicted shaft angles are also nearly identical across the speed range, until $\mu = 0.27$, where the swashplateless shaft angles level off (see Fig. 22b). The change in the predicted power of the swashplateless rotor can be explained by the rotor hub moments, which were forced to zero for the previous 3 dof targetted thrust trim solutions. Despite the change in the trim procedure, the trend of the power prediction is not altered from that originally seen with the refined TEF trailer wake model (in Figure 17). At low speed, the swashplateless power prediction is lower than the baseline, and as the forward flight speed increases, the prediction increases above the baseline power calculation.

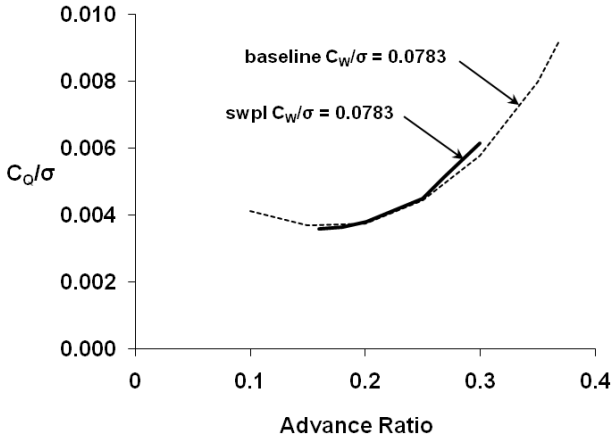

(a) Rotor Power

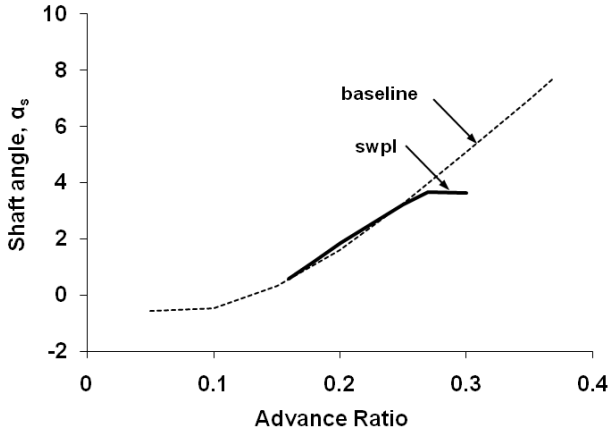

(b) Shaft Angle

Figure 22: Swashplateless Rotor in Forward Flight Compared to Baseline Rotor, TEF Trailer Wake Model, Vehicle Trim, $C_W/\sigma = 0.0783$

The flight condition is changed so that the weight coefficient is increased, and the performance of the swashplateless rotor is compared to the baseline UH-60A across the range of flight speed. The predictions for the baseline rotor at higher thrust levels were validated against flight test data obtained from the NASA/Army UH-60A Airloads Program, and previously published in a performance analysis of the rotor [20].

Trim solutions for the swashplateless rotor were obtained at two thrust levels, $C_W/\sigma = 0.0783$ and $C_W/\sigma = 0.0891$, and compared to the baseline rotor in Fig. 23. Figure 23 and Figure 24 compare the swashplateless power predictions at the two different thrust levels. As the thrust increases, the swashplateless predicted power curves increase at a nearly constant offset. This differs from the conventional rotor, for which the difference between the

power curves decreases as the forward flight speed increases. For $C_W/\sigma = 0.0891$ at low speed, $\mu = 0.13$, the prediction for the swashplateless rotor is 2% below that of the conventional rotor. As the forward flight speed increases, the predicted power rises with respect to the conventional rotor until at $\mu = 0.26$, there is a 13% increase. For the range of forward flight speed up to about $\mu = 0.22$, the swashplateless rotor trim position is very similar to the conventional rotor for both thrust levels, as shown in Fig. 24. Above that speed, the swashplateless predictions for rotor shaft angle fall below those for the conventional rotor. Figure 25 shows that at both thrust levels, $C_W/\sigma = 0.0783$ and $C_W/\sigma = 0.0891$, the flap control angles for the swashplatess rotor show a steady decrease in the mean flap angle as the advance ratio increases, and a corresponding increase in the half peak-to-peak (hpp) angles. Note that as the thrust increased from $C_W/\sigma = 0.0783$ to $C_W/\sigma = 0.0891$, the maximum forward flight speed for which trim solutions were obtained decreased.

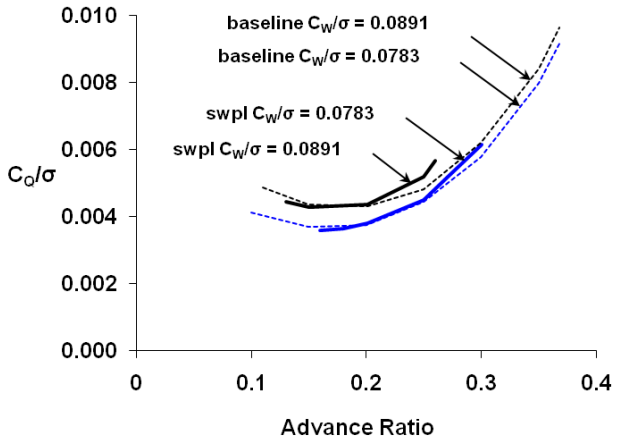

Figure 23: Effect of Increasing Thrust on Predicted Power of Swashplateless Rotor in Forward Flight, TEF Trailer Wake Model, Vehicle Trim

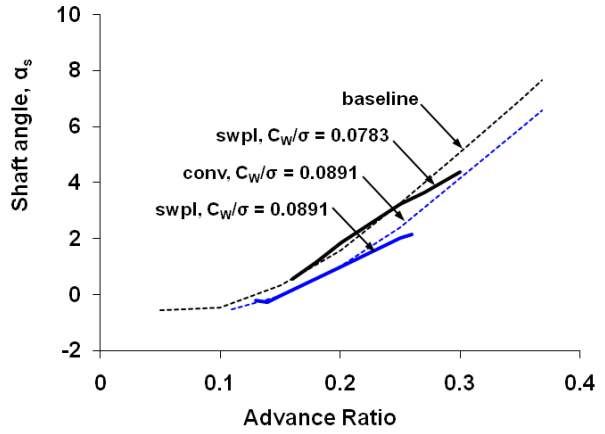

Figure 24: Effect of Increasing Thrust on Predicted Shaft Angles of Swashplateless Rotor in Forward Flight, TEF Trailer Wake Model, Vehicle Trim

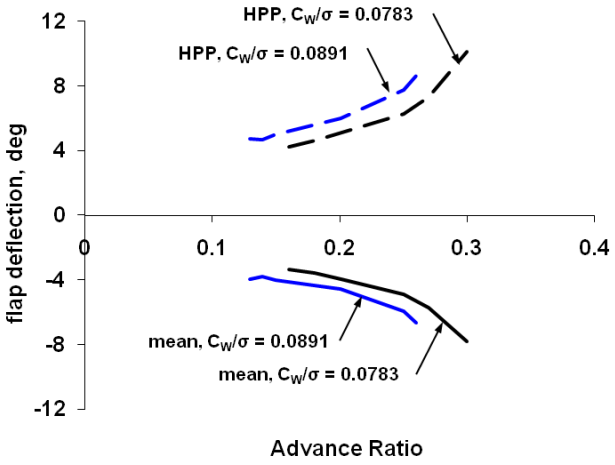

Figure 25: Effect of Increasing Thrust on Flap Control Angles of Swashplateless Rotor in Forward Flight, TEF Trailer Wake Model, Vehicle Trim

Effect of Flat Plate Area on Swashplateless Rotor

The original UH-60A production vehicle had an equivalent flat plate area of 26 ft^2 for the fuselage drag. The sixth-year production vehicle tested in the Airloads Program is equipped with External Stores Support System (ESSS) fairings, accessories to the de-icing system and a wire-strike kit that increase the drag area significantly [20]. The addition of the additional stores and systems changed the UH-60A from a relatively "clean" drag profile to one that can better be described as "dusty" [21] for its gross weight. For this investigation, a value of 35 ft^2 has been used throughout as an estimate of the fuselage drag for both the conventional and swashplateless rotors.

Figure 26 shows the equivalent flat plate area for helicopters at a range of gross weights, along with a typical breakdown of the sources of parasite drag. The hub is assigned a value of 30% of the total fuselage drag; removing the swashplate should reduce the hub drag significantly. Accordingly, for this study the swashplateless rotor is examined for the effect of reducing the parasite drag to 90% and 80% of the initial value. Reducing the drag by 10% or 20% simulates the removal of the swashplate, and may indicate a performance advantage achievable with the swashplateless configuration.

In Figure 27, each 10% decrease in the parasite drag results in a 2.5% decrease in the power prediction for the swashplateless rotor, so that the case with 80% drag has a power prediction 5% lower than the 100% drag case. This moderate reduction in predicted power is accompanied by a large change in the rotor shaft angle in Figure 28. At $\mu = 0.25$, the shaft angle of the 80% drag case has decreased 23% from the position for the 100% drag case. The flap control angles are not significantly affected by decreasing drag, as shown in Fig. 29. This is a consequence of the rotor trimming at different shaft angles. If the shaft angles were held constant and the thrust and hub moments prescribed, larger changes in flap control angles would result.

The swashplateless rotor used throughout this performance study is nearly identical to the UH-60A. The torsional frequency of the rotor was lowered by reducing the

stiffness of the root pitch spring, and trailing edge flaps were added to the blades. The blade airfoils, selected to maximize the performance and maneuverability of the baseline rotor, are unchanged. It is seen that the swashplateless rotor, operating with a different distribution of angle of attack due to the lowered torsional frequency, uses these airfoils less efficiently. The rotor lift-to-drag ratio in Fig. 30 was calculated for the baseline rotor and for the swashplateless rotor at 100%, 90% and 80% parasite drag. For the range of forward flight speed from $\mu = 0.1$ to 0.25, the lift-to-drag ratio of the swashplateless rotor is very close to the baseline rotor, regardless of decreases in parasite drag. However the baseline rotor sees a maximum lift-to-drag ratio near $\mu = 0.30$, while the ratio for the swashplateless rotor declines sharply after $\mu = 0.25$.

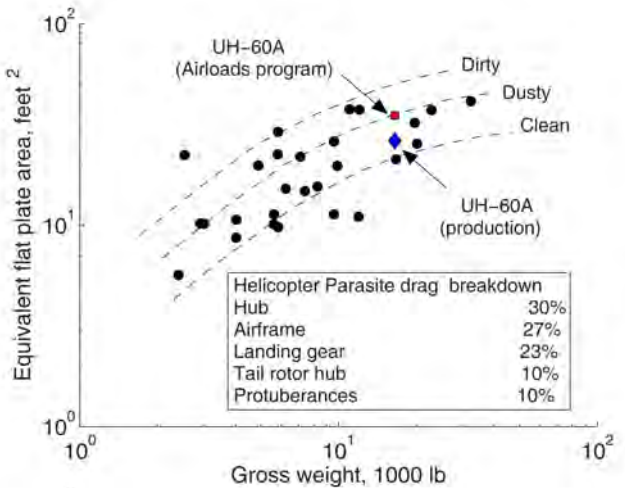

Figure 26: Distribution of Parasite Drag (Ref. [21])

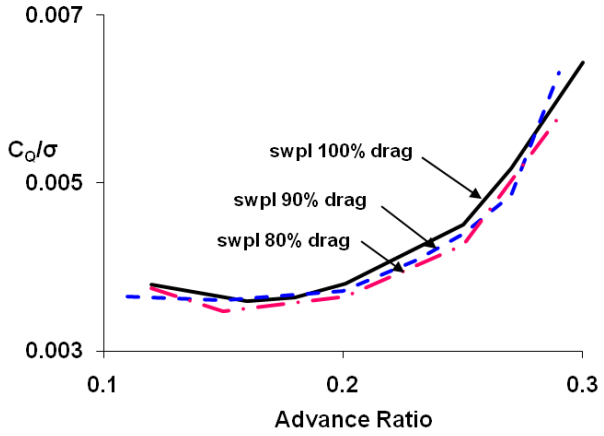

Figure 27: Effect of Decreasing Parasite Drag on Predicted Power of Swashplateless Rotor in Forward Flight, TEF Trailer Wake Model, Vehicle Trim, $C_W/\sigma = 0.0783$

CONCLUSIONS

The predictions of main rotor power and rotor lift-to-drag ratio are dependent on the accuracy of aerodynamic model of the comprehensive analysis. For the current work, the aerodynamic model was refined to include the effect of the

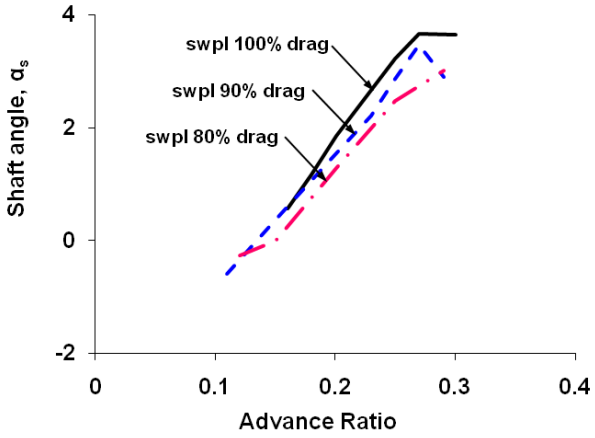

Figure 28: Effect of Decreasing Parasite Drag on Predicted Shaft Angles of Swashplateless Rotor in Forward Flight, TEF Trailer Wake Model, Vehicle Trim, $C_W/\sigma = 0.0783$

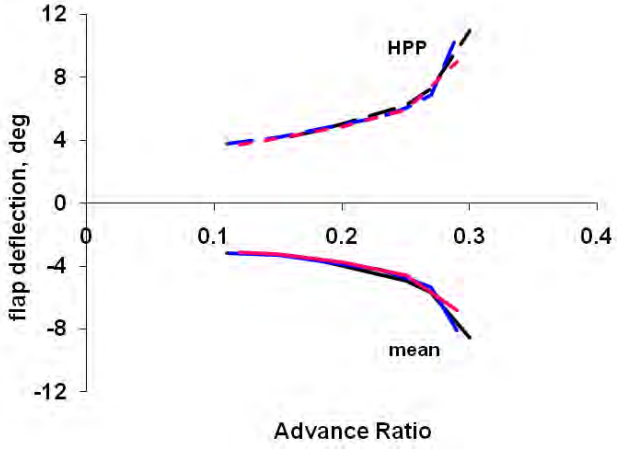

Figure 29: Effect of Decreasing Parasite Drag on Flap Control Angles of Swashplateless Rotor in Forward Flight, TEF Trailer Wake Model, Vehicle Trim, $C_W/\sigma = 0.0783$

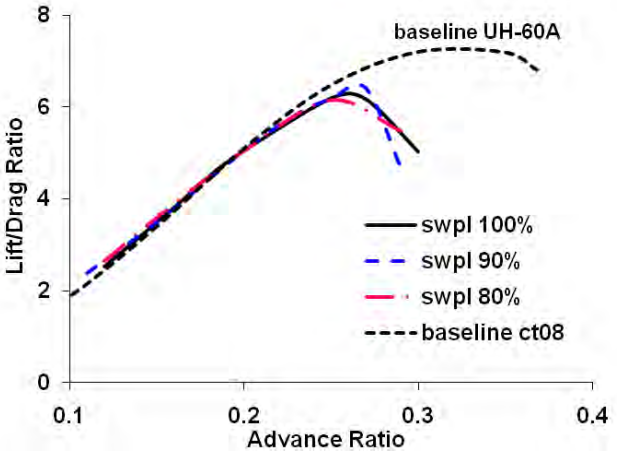

Figure 30: Effect of Decreasing Parasite Drag on Lift-to-Drag Ratio of Swashplateless Rotor in Forward Flight, TEF Trailer Wake Model, Vehicle Trim, $C_W/\sigma = 0.0783$

trailing edge flap through airfoil table lookup and through the wake model. The swashplateless rotor used in every performance study is a variant of the UH-60A, where the torsional frequency has been reduced from 4.3/rev to 2.0/rev by reducing the stiffness of the root pitch spring. The trailing edge flap on each blade is 0.15c in size, has no aerodynamic balance and spans 0.40 of the blade radius. This flap configuration was selected to facilitate actuator performance through the minimization of flap deflection and hinge moment. The purpose of the current study is to assess the impact of this configuration on rotor performance, and the focus is not on modifying the swashplateless rotor to improve performance. The following conclusions are drawn from the performance study:

1. In hover, the swashplateless rotor requires less power than the conventional rotor, for a limited range of thrust at each index angle. A high index angle produces an increase in figure of merit (FM) compared to the baseline, at some thrust levels. Beyond the thrust level at which the maximum FM is produced, the predicted power increases rapidly compared to the baseline rotor and the figure of merit drops. This appears to limit the upper range of thrust at which the swashplateless rotor operates efficiently in hover.

2. The wake model used to analyze the swashplateless rotor has a significant effect on the prediction of rotor power in forward flight. A uniform inflow model produces a predicted power curve that follows the trend of the baseline (swashplate) rotor. This model might be sufficient for relative comparisons between rotors. A refined free wake model that accounts for the trailed vorticity from the trailing edge flap produces rotor power predictions that also follow the trend of the baseline rotor. The refined model indicates that the swashplateless rotor may require less power than the baseline at low speed, and more at high speed. This conclusion depends on the rotor models having identical configurations (and parasitic drag), except for torsional frequency and trailing edge flaps.

3. The flap deflections required to trim the swashplateless rotor in forward flight vary with the inflow model used in the comprehensive analysis. Using 3 degree of freedom rotor trim and a target thrust level of $c_T/\sigma = 0.0783$, the three inflow models used required the following flap deflections to trim:

   - Uniform inflow resulted in mean flap deflections of $-4°$ to $-10°$, and half peak-to-peak cyclic deflections of $3°$ to $11.5°$.
   - The free wake model with a single tip vortex resulted in mean flap deflections of $-6°$ to $-9°$, and half peak-to-peak cyclic deflections of $7.5°$ to $11.5°$.
   - The modified free wake model with trailers at the flap boundaries resulted in mean flap deflections of $-3°$ to $-6.5°$, and half peak-to-peak cyclic deflections of $3°$ to $8°$.

4. Solutions can be calculated for the swashplateless rotor in full vehicle trim across the range of forward flight speed. Trim solutions obtained for the rotor using the modified wake model result in power predictions that closely follow the power prediction of the baseline rotor. At low speed, $\mu = 0.16$, the swashplateless prediction is 1% lower than the baseline. The difference between the predictions increases slowly until at $\mu = 0.30$, the swashplateless power is 11% higher than the baseline. The predicted rotor shaft angles for the swashplateless rotor show good agreement with the predictions for the baseline rotor across the range of forward flight speed until $\mu = 0.30$. The mean trailing edge flap deflections range from $-3°$ to $-9°$. The half peak-to-peak flap deflections range from $4°$ to $11°$.

5. The swashplateless UH-60A rotor can be trimmed at a higher weight level, $C_W/\sigma = 0.0891$. The increase in predicted rotor power is similar to the trend seen for the baseline, but the maximum speed at which a solution could be obtained is reduced to $\mu = 0.26$. The flap control angles increase with the increased thrust, but follow the same trend as the solutions found for $C_W/\sigma = 0.0783$. Trim solutions could not be obtained for vehicle weights higher than $C_W/\sigma = 0.0891$.

6. Except where noted explicitly, the equivalent flat plate area is held constant in comparisons between the baseline and swashplateless rotors for most of this investigation. Accordingly, the power predictions shown for the swashplateless rotor are conservative. When the parasitic drag was reduced 20% from the baseline, the swashplateless power prediction decreased 5%, with a concurrent decrease of the rotor shaft angle of 23%.

7. The rotor lift-to-drag ratio was calculated for the swashplateless rotor at different increments of parasitic drag, and compared to the baseline rotor (with unchanged parasitic drag). For all increments of parasite drag, the maximum lift-to-drag ratio of the swashplateless rotor occurs at or below $\mu = 0.26$. This is in contrast to the baseline rotor, where the maximum lift-to-drag ratio occurs near $\mu = 0.35$. Up to $\mu = 0.26$, the swashplateless ratio follows the baseline rotor closely, then decreases rapidly. Beyond $\mu = 0.30$, trim solutions are difficult to obtain for the swashplateless rotor. These results indicate that at higher advance ratios, the swashplateless UH-60A operates less efficiently than the baseline rotor.

REFERENCES

[1] J. Falls, A. Datta, and I. Chopra. Design and analysis of trailing-edge flaps and servotabs for primary control. In *American Helicopter Society 63rd Annual Forum Proceedings*, Virginia Beach, VA, May 2007. AHS.

[2] J. Falls, A. Datta, and I. Chopra. Integrated trailing-edge flaps and servotabs for helicopter primary control. In *American Helicopter Society 62nd Annual Forum Proceedings*, Phoenix, AZ, May 2006. AHS.

[3] K. Noonan, W. Yeager, J. Singleton, M. Wilbur, and P. Mirick. Wind tunnel evaluation of a he-

licopter main-rotor blade with slotted airfoils at the tips. Technical Report NASA-TP-2001-211260, NASA Langley Research Center, Hampton, VA, December 2001.

[4] A. Gagliardi and G.N. Barakos. Analysis and design of a flap-equipped low-twist rotor for hover. *Journal of Aircraft*, 46(1):74–84, January-February 2009.

[5] B. Glaz, P. Friedmann, and L.Liu. Active/passive vibration reduction and performance enhancement of helicopter rotors at high advance ratios. In *American Helicopter Society 64th Annual Forum Proceedings*, Montreal, Canada, May 2008. AHS.

[6] L. Liu, P. Friedmann, I. Kim, and D. Bernstein. Rotor performance enhancement and vibration reduction in presence of dynamic stall using actively controlled flaps. *Journal of the American Helicopter Society*, 53(4):338–350, October 2008.

[7] H. Yeo. Assessment of active controls for rotor performance enhancement. *Journal of the American Helicopter Society*, 53(2):152–163, April 2008.

[8] J. Falls, A. Datta, and I. Chopra. Integrated trailing-edge flaps and servotabs for helicopter primary control. *Journal of the American Helicopter Society*, 55 (3):032005, July 2010.

[9] A. Datta and I. Chopra. Validation and understanding of UH-60A vibratory loads in steady level flight. *Journal of the American Helicopter Society*, 49(3): 271–287, July 2004.

[10] A. Datta and I. Chopra. Validation of structural and aerodynamic modeling using UH-60A airloads program data. *Journal of the American Helicopter Society*, 51(1):43–58, January 2006.

[11] D.H. Hodges and E. Dowell. Nonlinear equations of motion for the elastic bending and torsion of twisted nonuniform rotor blades. Technical Report TN D-7818, NASA, 1974.

[12] D.H. Hodges, R. Ormiston, and D. Peters. On the nonlinear deformation geometry of euler-bernoulli beams. Technical Report TR 1566, NASA, 1980.

[13] T. Theodorsen and I.E. Garrick. Nonstationary flow about a wing-aileron-tab combination including aerodynamic balance. Technical Report 736, NACA, 1942.

[14] K. Duraisamy. *Studies in Tip Vortex Formation, Evolution and Control*. PhD thesis, University of Maryland, College Park, 2005.

[15] T. H. Pulliam and D. S. Chaussee. A diagonal form of an implicit approximate factorization algorithm. *Journal of Computational Physics*, 39(1):347–363, February 1981.

[16] P.R. Spalart and S.R. Allmaras. A one equation turbulence model for aerodynamics flow. *AIAA*, (92-0439):1–22, 1992.

[17] M. Smith, M. Potsdam, T.-C. Wong, J. Baeder, and S. Phanse. Evaluation of computational fluid dynamics to determine two-dimensional airfoil characteristics for rotorcraft applications. *Journal of the American Helicopter Society*, 51(1):70–79, January 2006.

[18] A. Hassan, F. Straub, and K. Noonan. Experimental/numerical evaluation of integral trailing edge flaps for helicopter rotor applications. *Journal of the American Helicopter Society*, 50(1):3–17, January 2005.

[19] A. Bagai and J. Leishman. Rotor free-wake modeling using a pseudo-implicit technique - including comparisons with experimental data. *Journal of the American Helicopter Society*, 40(3):29–41, July 1995.

[20] H. Yeo, W.G. Bousman, and W. Johnson. Performance analysis of a utility helicopter with standard and advanced rotors. *Journal of the American Helicopter Society*, 49(3):250–270, July 2004.

[21] R.M. Carlson. Helicopter performance - transportation's latest chromosome: The 21st annual Alexander A. Nikolsky lecture. *Journal of the American Helicopter Society*, 47(1):3–17, January 2002.